



Dynamic shear characteristics of titanium alloy Ti-6Al-4V at large strain rates by the split Hopkinson pressure bar test



Tianfeng Zhou^{a,*}, Junjie Wu^b, Jiangtao Che^b, Ying Wang^b, Xibin Wang^a

^a Key Laboratory of Fundamental Science for Advanced Machining, Beijing Institute of Technology, No.5 Zhongguancun South Street, Haidian District, Beijing, 100081, PR China

^b School of Mechanical Engineering, Beijing Institute of Technology, No.5 Zhongguancun South Street, Haidian District, Beijing, 100081, PR China

ARTICLE INFO

Article History:

Received 22 May 2016

Revised 23 May 2017

Accepted 17 June 2017

Available online 20 June 2017

Keywords:

SHPB test

Strain rate

Shear band

Johnson–Cook constitutive model

FEM simulation

ABSTRACT

The focus of this paper is the dynamic shear characteristics of titanium alloy Ti-6Al-4V at large strain rates. Dynamic load testing of titanium alloy Ti-6Al-4V are performed by the split Hopkinson pressure bar (SHPB) at different strain rates, which involve the SHPB compression test and the SHPB shear test. The material behaviour during the tests are measured and recorded. The strain rates for the compression and shear tests range from $5.0 \times 10^2 \text{ s}^{-1}$ to $9.0 \times 10^3 \text{ s}^{-1}$ and $1.0 \times 10^4 \text{ s}^{-1}$ to $3.0 \times 10^5 \text{ s}^{-1}$, respectively. The effect of competing mechanisms—strain rate hardening and thermal softening—on the adiabatic shear band is analysed. A size effect on shear band width is also found. According to the results, a modified Johnson–Cook (J–C) constitutive model is applied to tests at an ultrahigh strain rate. Furthermore, a finite element method (FEM) simulation is conducted to validate different aspects of the methodology. The SHPB shear test is confirmed as a process of pure shear. A comparison of the shear stress-strain curves from the mechanical tests and simulation show good agreement based on the modified J–C constitutive model.

© 2017 Elsevier Ltd. All rights reserved.

1. Introduction

The titanium alloy Ti-6Al-4V (also named TC4) is widely used in aerospace, shipbuilding, chemicals, weapons and other industrial fields because of its low density, high strength, excellent resistance to corrosion, and heat resistance [1]. In recent years, the strength of titanium alloy Ti-6Al-4V has been tested at high strain rates such as through high speed machining or compression forming [2]; dynamic mechanical property testing is important to establish the constitutive model of the Ti-6Al-4V alloy.

Material property testing has been extensively studied to characterize different mechanical responses, including strength, fatigue, creep, constitutive properties, fracture toughness, and phase transformation. [3]. Previous studies on the mechanical behaviour of the Ti alloy are typically quasi-static or at low strain rate. Early investigations of the material strength under unstable deformation focused on the sensitivity of quasi-static shear localization where the localized deformation was considered a bifurcation behaviour [4]. Pei and Li studied the quasi-static tensile mechanical properties of TC6 alloy under a low direct current at a strain rate of $1.67 \times 10^{-4} \text{ s}^{-1}$ and found that thermal stress reduced the yield strength of the TC6 alloy [5]. Mohammad et al. investigated the compressive deformation behaviour of electron beam melting (EBM) processed titanium

alloy (Ti-6Al-4V) parts under high strain loading conditions. The dynamic compression tests were carried out for a strain rate range of $1.0 \times 10^{-3} \text{ s}^{-1}$ to $1.0 \times 10^3 \text{ s}^{-1}$ [6]. Wang provided the Johnson–Cook (J–C) constitutive model for TC17 from uniaxial quasi-static and dynamic compression tests at high strain rate. In addition, Wang found that the influence of thermal softening is greater than the influence of strain and strain rate hardening [7]. However, the mechanical properties of titanium alloy at large strain rates—over $1.0 \times 10^4 \text{ s}^{-1}$ —and the relationship between the strain rate hardening effect and thermal softening effect remains unknown.

Based on previous mechanical property studies of Ti alloy, the split Hopkinson pressure bar (SHPB) test is selected for the dynamic load testing of Ti-6Al-4V alloy in this paper. To study the dynamic characteristics of titanium alloy Ti-6Al-4V at large strain rate, the SHPB test is divided into two parts: the SHPB compression test [8] at strain rates in the range of $5.0 \times 10^2 \text{ s}^{-1}$ to $9.0 \times 10^3 \text{ s}^{-1}$ and the SHPB shear test [9] at strain rates in the range of $1.0 \times 10^4 \text{ s}^{-1}$ – $3.0 \times 10^5 \text{ s}^{-1}$. The competing mechanisms of the strain rate hardening effect and thermal softening effect were analysed, and the size effect of the shear band width is also identified. Based on the SHPB test, the J–C constitutive model at an ultrahigh strain rate is modified. The validation of this methodology through finite element analysis (FEA) is addressed later in this paper. Particularly, the experimental and simulation shear stress-strain curves were compared. The results showed good agreement at an ultrahigh strain rate based on a modified J–C constitutive model.

* Corresponding author.

E-mail address: zhoutf@bit.edu.cn (T. Zhou).

2. Methodology

2.1. Introduction of titanium alloy Ti-6Al-4V

The chemical composition of titanium alloy Ti-6Al-4V is shown in Table 1 [10]. The Ti-6Al-4V alloy is a two-phase $\alpha+\beta$ alloy that has high strength, superior stability, toughness, plasticity and high temperature deformation. Strength and hardness are important constituents when evaluating the mechanical properties of materials. The physical and mechanical properties of Ti-6Al-4V are shown in Table 2 [11].

2.2. SHPB test principle

A dynamic loading test is performed using a split Hopkinson pressure bar (SHPB) system, which consists of a striker bar, incident bar, transmission bar and an energy absorber. The SHPB diagram is shown in Fig. 1. The specimen is placed between the incident and transmission bars. At first, the velocity of the striker bar, which determines the strain rate, is driven by the cylinder pressure. The striker bar hits the incident bar with a constant speed in the annular tube and generates the incident wave that is transmitted throughout the bar. Then, the specimen is compressed, deformed or fractured

Table 1
Chemical composition of titanium alloy Ti-6Al-4V (mass fraction, %).

Al	V	Fe	C	N	H	O	Ti
6.16	3.95	0.03	0.04	0.014	0.005	0.06	Bal.

Table 2
Physical and mechanical properties of titanium alloy Ti-6Al-4V.

Density (kg/m ³)	4500
Melting point (°C)	1668
Specific heat (J/kg•°C)	612
Thermal conductivity (W/m•°C)	7.955
Elasticity modulus (GPa)	114
Poisson ratio	0.34

when the stress wave reaches the interface between the incident bar and the specimen. Meanwhile, part of the incident wave becomes a transmission wave propagating through the transmission bar, and the other part of the incident wave becomes a reflected wave transferring towards the incident bar with the opposite velocity. Finally, the energy absorber acts as a buffer. At this stage, two strain gauges, which are stuck on the incident bar and the transmission bar, separately, collect the pulse signals of the stress wave [12]. The striker, incident and transmission bars have the same diameter ($\phi 13$ mm) and the incident and transmission bars have the same length (1 m).

Regarding strain rate, five intervals are typically used to study the material properties: quasi-static ranges from $1.0 \times 10^{-4} \text{ s}^{-1}$ to $1.0 \times 10^{-2} \text{ s}^{-1}$, low strain rate ranges from $1.0 \times 10^{-2} \text{ s}^{-1}$ to $1.0 \times 10^{-1} \text{ s}^{-1}$, the medium strain rate ranges from $1.0 \times 10^{-1} \text{ s}^{-1}$ to $1.0 \times 10^2 \text{ s}^{-1}$, the high strain rate ranges from $1.0 \times 10^2 \text{ s}^{-1}$ to $1.0 \times 10^4 \text{ s}^{-1}$ and the ultrahigh strain rate is beyond $1.0 \times 10^4 \text{ s}^{-1}$ [13]. As shown in Fig. 2, the strain rate range of $5.0 \times 10^2 \text{ s}^{-1}$ and $9.0 \times 10^3 \text{ s}^{-1}$ can be achieved by the SHPB compression test, and a higher strain rate range of $1.0 \times 10^4 \text{ s}^{-1}$ – $3.0 \times 10^5 \text{ s}^{-1}$ can be achieved by the SHPB shear test.

2.3. SHPB compression test

The dynamic compression test of titanium alloy Ti-6Al-4V is performed by SHPB. Different nominal strain rates from $5.0 \times 10^2 \text{ s}^{-1}$ to $9.0 \times 10^3 \text{ s}^{-1}$ were obtained by controlling the velocity of the striker bar. The dimensions selected for the standard specimen were based on the size of the bar. Specifically, the diameter of the specimen is 0.8 times that of the bar to ensure that the specimen achieved a true strain of 30% before the diameter of specimen exceeded the diameter of the bar [14]. After calculation, the specimen is determined to have a diameter of $\phi 5$ mm and a length of 5 mm.

In accordance with the SHPB experimental principles, the incident wave, reflected wave and transmission wave produce three different strains, ϵ_I (incident strain), ϵ_R (reflected strain), ϵ_T (transmission strain), respectively, on both the incident bar and transmission bar. Based on the one-dimensional elastic wave theory, strain rate, strain and stress are given by Eqs. (1), (2), and (3), respectively [15].

$$\sigma = \frac{A_h}{A_s} E \epsilon_T \quad (1)$$

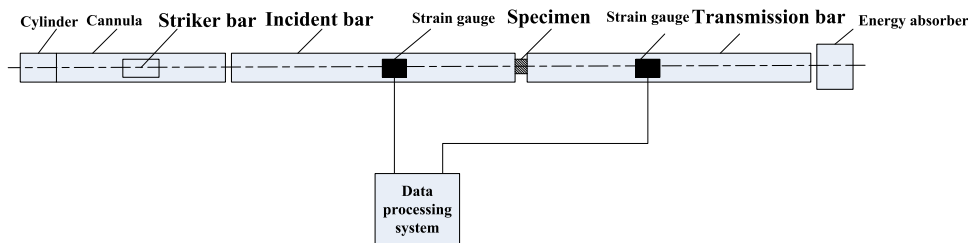


Fig. 1. Components of SHPB.

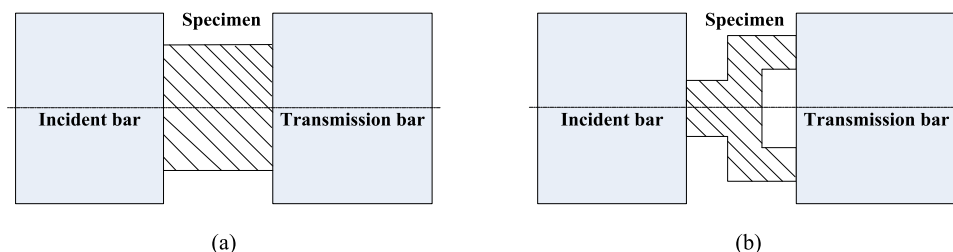


Fig. 2. Schematic of the specimen loading: (a) SHPB compression test and (b) SHPB shear test.

$$\varepsilon = \frac{-2C_0}{L_s} \int \varepsilon_R dt \quad (2)$$

$$\dot{\varepsilon} = \frac{-2C_0}{L_s} \varepsilon_R(t) \quad (3)$$

In these equations, σ represents yield stress, ε represents strain, $\dot{\varepsilon}$ represents strain rate, $C_0 = \sqrt{E/\rho}$ represents the elastic longitudinal wave velocity of the bars; ρ represents the density of the bars; A_h and E represent cross-section and elastic modulus of the bars, respectively; and L_s and A_s represent the initial length and cross-section of the specimen, respectively.

2.4. SHPB shear test

The specimen is redesigned to study the strength of titanium alloy Ti-6Al-4V in the ultrahigh strain rate range. Becze [16] designed a pure shear hat-shaped specimen based on the design of Meyer and Manwaring [17], which is shown in Fig. 3. There is a simulated shear band (the shadow part in Fig. 3) on the hat-shaped specimen, which is a state of pure shear in the loading process. A hat-shaped specimen is widely used in similar research of the adiabatic shear in different materials because of its simple structure. The greatest difference between the initial and improved hat-shaped specimens are d_1 and d_2 , respectively. The cap cylinder of the improved hat-shaped specimen is smaller than the hat bore size ($d_1 < d_2$), which is different for the dimensions of the initial hat-shaped specimen ($d_1 > d_2$). Shear fracture develops more easily in the improved specimen compared with the initial hat-shaped structure. The dimensions of the improved specimen are as follows: $d_1 = 4.6$ mm, $d_2 = 5$ mm, and $d_3 = 9$ mm. The specimen height is constant ($a = 1.5$ mm), and the shear band widths ($b = 400$ μ m, 200 μ m, 50 μ m) are designed.

According to the one-dimensional elastic wave theory, shear stress, shear strain and shear strain rate can be obtained by processing the collected strain signal data [18].

$$\tau_s = \frac{2EA\varepsilon_T}{\pi(d_2 + d_3)(h_2 - h_3)} \quad (4)$$

$$\gamma_s = -\frac{4C_0}{d_2 - d_3} \int \varepsilon_R dt \quad (5)$$

$$\dot{\gamma}_s = -\frac{4C_0}{d_2 - d_3} \varepsilon_R \quad (6)$$

In these equations, τ_s represents the shear stress, γ_s represents the shear strain, $\dot{\gamma}_s$ represents the shear strain rate, $C_0 = \sqrt{E/\rho}$ represents the elastic longitudinal wave velocity of the bars, and ρ represents the density of bars.

Table 3
SHPB shear test results.

Test number	Shear band width (b , μ m)	Shear strain rate ($\dot{\gamma}_s$, $\times 10^4$ s $^{-1}$)	Specimen state after tests
T1	400	1.0	Fractured
T2	400	3.0	Fractured
T3	400	5.0	Fractured
T4	200	1.5	Fractured
T5	200	3.0	Fractured
T6	200	5.0	Fractured
T7	200	10.0	Fractured
T8	50	5.0	Non-fractured
T9	50	10.0	Non-fractured
T10	50	15.0	Fractured
T11	50	30.0	Fractured

3. Experimental test and constitutive modelling

3.1. Experimental results of SHPB tests

For the SHPB shear tests, the nominal shear strain rates are designed according to three shear band widths, and the results are shown in Table 3.

The pulse signals of the stress wave collected by the strain gauges are shown in Fig. 4. The hat-shaped specimen of T3 ($b = 400$ μ m, $\dot{\gamma}_s = 5.0 \times 10^4$ s $^{-1}$) fractured and the specimen of T8 ($b = 50$ μ m, $\dot{\gamma}_s = 5.0 \times 10^4$ s $^{-1}$) and T9 ($b = 50$ μ m, $\dot{\gamma}_s = 1.0 \times 10^5$ s $^{-1}$) experience large plastic deformation, which is shown in Fig. 5. After the specimen fractured, the incident bar moved forward and then hit the lower half of the hat-shaped specimen (i.e., annulus part). This process is considered the compression test. However, based on the recorded data, the residue from compression is very low, and its influence on the specimen is therefore neglected [19]. In addition, the velocity of specimen deformation is higher than the velocity of the incident bar; hence, the condition of reloading the specimen is avoided. Furthermore, the length of two pressure bars is sufficient to ensure that there is no reflection in the waveform acquisition process; accordingly, Eq. (7) is required.

$$|\varepsilon_T| + \varepsilon_R = \varepsilon_I \quad (7)$$

The pulse signals of the SHPB shear test for the T3 and T9 testing conditions are shown in Fig. 4(a) and (b), respectively. In Fig. 4(a), it is observed that the incident wave transferred to the specimens at 292 μ s (point A). Then, a part of the stress wave is transferred to form the transmission wave, and the other part of the stress wave forms the reflected wave. At 319 μ s, the signal starts to drop, which implies that the shear band in the specimen has evolved into an

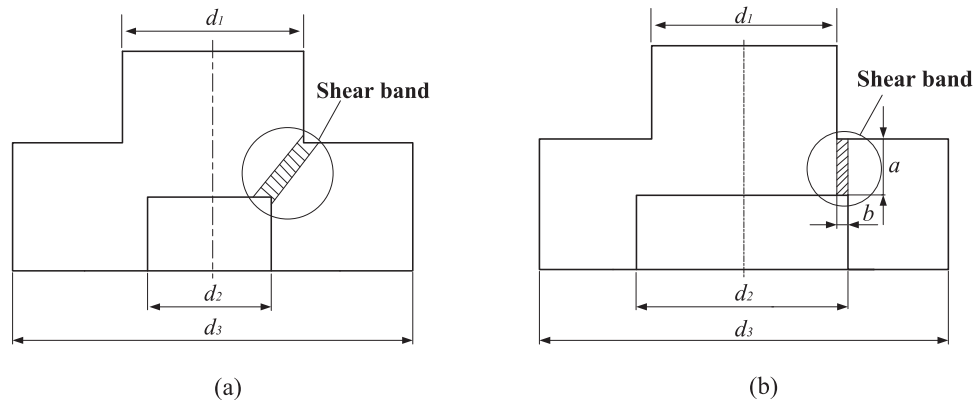


Fig. 3. Comparison between (a) the initial and (b) the improved specimen.

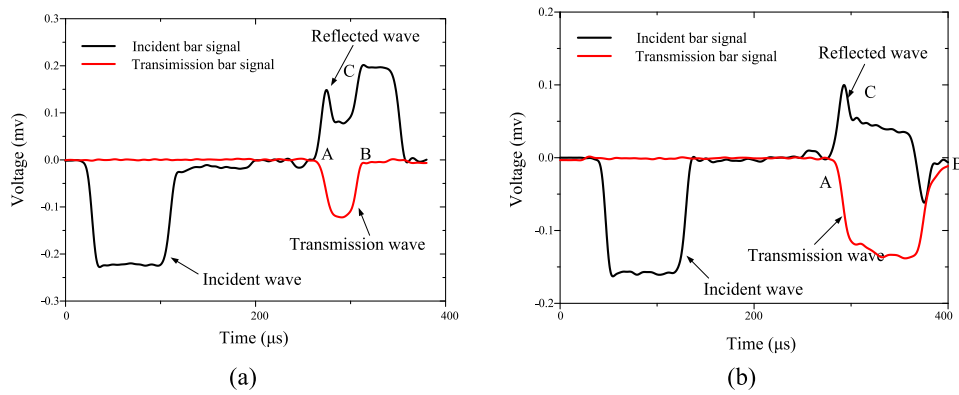


Fig. 4. Pulse signals of SHPB shear test under different testing conditions: (a) T3 ($b = 400 \mu\text{m}$, $\dot{\epsilon}_s = 5.0 \times 10^4 \text{ s}^{-1}$) and (b) T9 ($b = 50 \mu\text{m}$, $\dot{\epsilon}_s = 1.0 \times 10^5 \text{ s}^{-1}$).

unstable stage; finally, fracture occurs at $343 \mu\text{s}$ (point B). At the same time, the maximum signal of the reflected stress wave is achieved (point C). The duration of the transmission stress wave is $51 \mu\text{s}$, which is shorter than the incident wave. Hence, it is concluded that this specimen fractured under the effect of the first compression wave. The initial and fractured specimens are shown in Fig. 5(a). The specimen does not fracture with a shear band width of $50 \mu\text{m}$ and $\dot{\epsilon}_s$ of $1.0 \times 10^5 \text{ s}^{-1}$, which is shown in Fig. 5(b). At this condition, the duration of the transmission wave is close to the incident wave in Fig. 4(b). Thus, it is deduced that large plastic deformation occurs only in the specimen in condition T9.

To study the dynamic characteristic of titanium alloy Ti-6Al-4V under high and ultrahigh strain rates, stress–strain curves from the SHPB compression and shear tests are compared. The true stress–strain curves of the cylindrical specimens under different strain rates varying from $5.0 \times 10^2 \text{ s}^{-1}$ to $9.0 \times 10^3 \text{ s}^{-1}$ can be seen in Fig. 6, and the ultimate stress are shown in Table 4. The results show that the ultimate stress of the material increases as the strain rate increases. When the strain rate changes from $5.0 \times 10^2 \text{ s}^{-1}$ to $9.0 \times 10^3 \text{ s}^{-1}$, the ultimate stress increases from 1359 MPa to 1576 MPa (an increase of 15.98%), owing to the strain rate hardening effect. Moreover, when the strain rate is higher than $1.0 \times 10^3 \text{ s}^{-1}$, the plastic stage is more obvious for the titanium alloy Ti-6Al-4V.

The shear stress–strain curves from SHPB shear testing of titanium alloy Ti-6Al-4V with three different shear band widths under an ultrahigh strain rate (T1~T11) can be seen in Fig. 7. The ultimate shear stress under different test conditions is shown in Table 5.

From Table 5 it can be seen that the ultimate shear stress increases and then decreases as the shear strain rate increases. There is a critical shear strain rate in this trend, which is different for the various shear band widths. The critical strain rate for $400 \mu\text{m}$ and $200 \mu\text{m}$ is between $3.0 \times 10^4 \text{ s}^{-1}$ and $5.0 \times 10^4 \text{ s}^{-1}$, and the critical strain rate for $50 \mu\text{m}$ is between $1.0 \times 10^5 \text{ s}^{-1}$ and $1.5 \times 10^5 \text{ s}^{-1}$. When the initial shear strain rate is relatively low, the ultimate shear stress increases as the shear strain rate increases due to a strain rate hardening effect. It is suggested that the formation of the strain rate hardening effect is related to the interaction of dislocations. However, as the shear strain rate increases, the large accumulation of plastic deformation work (approximately 90%) turns to heat. The heat accumulates in the shear band of the specimen, and it is difficult to dissipate in a very short period of time. Hence, the adiabatic shear band appears. Generally, the increase in temperature will cause softening of the material, which is called the thermal softening effect. In conclusion, under the ultrahigh strain rate, the deformation of the material is the result of the competing strain rate hardening effect and thermal softening effect. When the strain rate is lower than the critical strain rate, strain rate hardening plays a dominant role in the

Table 4

Ultimate stress of specimen under high strain rate.

Strain rate ($\times 10^2 \text{ s}^{-1}$)	5.0	10.0	50.0	70.0	90.0
Ultimate stress (MPa)	1359	1449	1467	1527	1576



(a)



(b)

Fig. 5. Initial (up) and loaded (down) specimens under different testing conditions: (a) T3 ($b = 400 \mu\text{m}$, $\dot{\epsilon}_s = 5.0 \times 10^4 \text{ s}^{-1}$) and (b) T9 ($b = 50 \mu\text{m}$, $\dot{\epsilon}_s = 1.0 \times 10^5 \text{ s}^{-1}$).

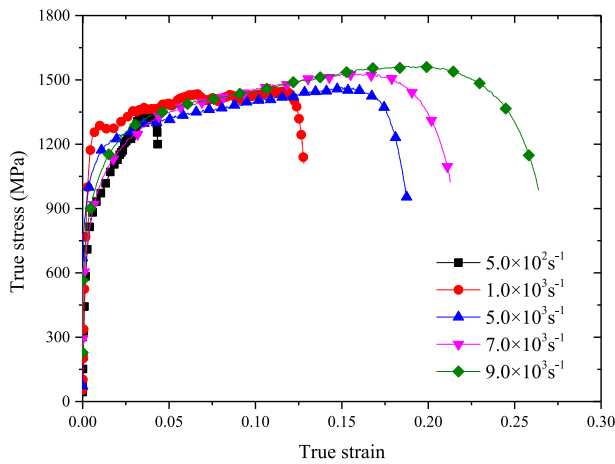


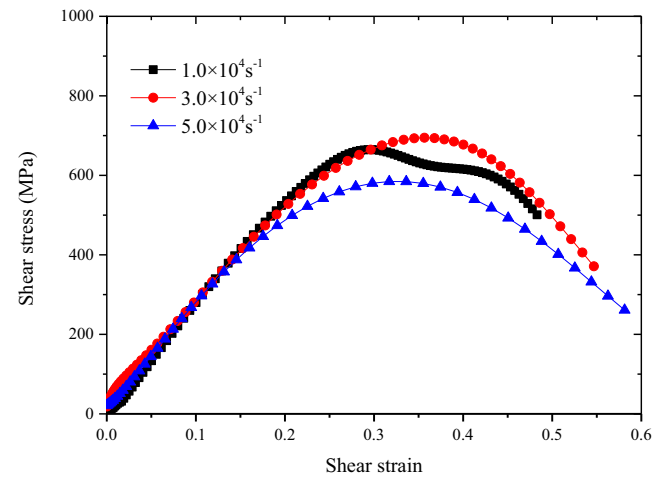
Fig. 6. True stress-strain curves of SHPB compression test under high strain rate.

competing mechanisms. On the other hand, in the SHPB shear test, the ultimate shear stress decreases with an increasing strain rate because the thermal softening effect is stronger than the strain rate hardening effect under the ultrahigh strain rate.

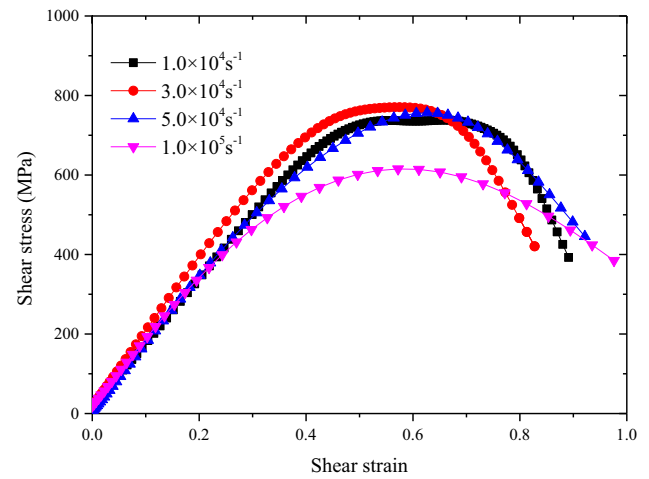
To study the influence of the shear band width, shear stress–strain curves were generated for different shear band widths at a strain rate of $5.0 \times 10^4 \text{ s}^{-1}$, which can be seen in Fig. 8. With an increasing shear band width, the shear strain corresponding to the ultimate shear stress increases; this is contrary to the theory that the mechanical properties of a material are not related to the material deformation geometry. In addition, the shear strain corresponding to the ultimate shear stress for a band width of $50 \mu\text{m}$ is much larger than for $400 \mu\text{m}$ and $200 \mu\text{m}$ which imply the size effect of the shear band width. As discussed above, in the process of the SHPB shear test, the material of the shear band is in the localized state of deformation and is accompanied by an adiabatic heat rise. With the shear strain and temperature increasing to a certain degree, the nucleation and dynamic recrystallization will appear. In this process, the plasticity and the hardening effect of Titanium Alloy Ti-6Al-4V may increase due to the change of grain morphology [20]. The specimen with smaller shear band will promote more local adiabatic heat due to the deformation is limited to a smaller region before fractured failure compared to the other larger band widths. It is more likely that the grain morphology of specimen with $50 \mu\text{m}$ shear band will change compared to those with $400 \mu\text{m}$ and $200 \mu\text{m}$. Because of this, the specimen with $50 \mu\text{m}$ shear band width has higher ultimate shear stress and the corresponding shear strain.

3.2. Microscope analysis of fractured surface

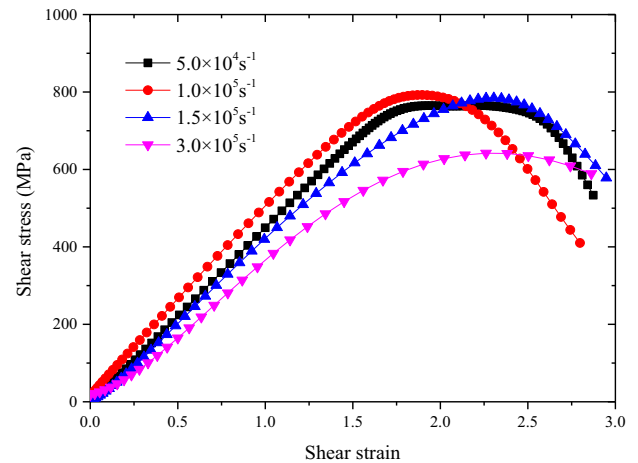
To study the fracture process of the SHPB test, scanning electron microscope (SEM) is used to observe the fractured surface and inner surface of the specimen after dynamic loading. The SEM images are shown in Fig. 9. In the SHPB shear tests, the fractured hat-shaped specimens are divided into two parts, as shown in Fig. 5(a) (down, cylinder part and annulus part). Fig. 9(a) shows the SEM photographs of the cylinder part that comprises the undeformed surface, transitional surface and fractured surface. In Fig. 10, two morphologies (dimples and cracks) are visible on the fractured surface. Particularly, several dimples are deep and accumulated, while others are shallow with an average diameter of approximately $10 \mu\text{m}$. The formation of dimples is identified as the plastic deformation [21]. A dimple is a type of micro void caused by plastic deformation in the micro cell range. Dimples experience the process of nucleation, growth and aggregation; finally, the dimples connect with each other, which results in surface fracture. Dimple



(a)



(b)



(c)

Fig. 7. Shear stress–strain curves of SHPB shear test with different shear band width: (a) $400 \mu\text{m}$, (b) $200 \mu\text{m}$, and (c) $50 \mu\text{m}$.

fracture is a ductile fracture with a high-energy absorption process [22]. The basic criterion of a ductile fracture mechanism is the presence of a honeycomb feature in the micromorphology of the fracture. In addition, the dimple size has a certain relationship with the

Table 5
Ultimate shear stress of specimen under the ultrahigh strain rate.

400 μm	Shear strain rate ($\times 10^4 \text{ s}^{-1}$)	1.0	3.0	5.0	
	Ultimate shear stress (MPa)	679	694	584	
200 μm	Shear strain rate ($\times 10^4 \text{ s}^{-1}$)	1.0	3.0	5.0	10.0
	Ultimate shear stress (MPa)	738	770	756	615
50 μm	Shear strain rate ($\times 10^4 \text{ s}^{-1}$)	5.0	10.0	15.0	30.0
	Ultimate shear stress (MPa)	764	792	784	641

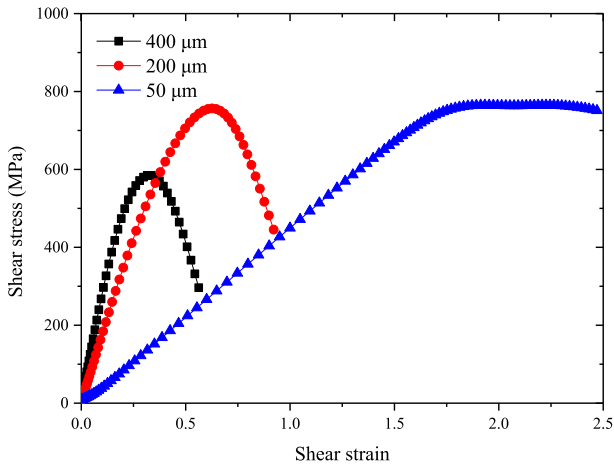


Fig. 8. Shear stress-strain curves of SHPB shear test at strain rate of $5.0 \times 10^4 \text{ s}^{-1}$.

plasticity of the material. As shown in Fig. 11, the average dimension of the dimples with a 50 μm shear band is larger than for a 400 μm shear band. The larger the dimple size is, the more serious the plastic deformation that occurs during dimple formation; hence, more energy is absorbed in the fracture process, which

implies that the specimen with a 50 μm shear band has better plasticity. This conclusion is in good agreement with the size effect of the shear band mentioned above.

The temperature in the local area within the shear band can instantly rise and surpass the critical point of phase transformation. In some cases, the local area of the material will be melted due to the high temperature [23]. Fig. 12 shows the SEM photographs of the melted microdamage in an area of the fractured surface and inner surface of the annulus part. The silver white light in Fig. 12(a) is the product of cooling and solidification of the material after melting of the fractured surface. The area in Fig. 12(b) may be caused by friction between the fragments and fracture surface, while the fractured surfaces are pliable by virtue of the instant temperature rise to the melting point in the shear band. Therefore, the deformation process at the ultrahigh strain rate is regarded as an adiabatic thermal process. The heat accumulates in the adiabatic shear band and results in a thermal softening effect on the Ti-6Al-4V alloy, as mentioned in Section 3.1.

3.3. Constitutive model modification

A thermo-viscoelastic constitutive model is used to describe the mechanical properties of the materials. The Johnson–Cook (J–C) constitutive model [24] is widely used because of the following features: simple structure, suitable for materials of various crystal structures and large deformation. The J–C constitutive model is shown in the following equation:

$$\sigma = [A + B\epsilon^n] \left[1 + C \ln \left(\frac{\dot{\epsilon}}{\dot{\epsilon}_0} \right) \right] \left[1 - \left(\frac{T - T_r}{T_m - T_r} \right)^m \right] \quad (8)$$

The following parameters appear in Eq. (8): T_r represents the reference temperature; T_m represents the melting point of the material; A , B , n , C , and m are undetermined parameters; n is the strain hardening coefficient of the material; and m is the thermal softening

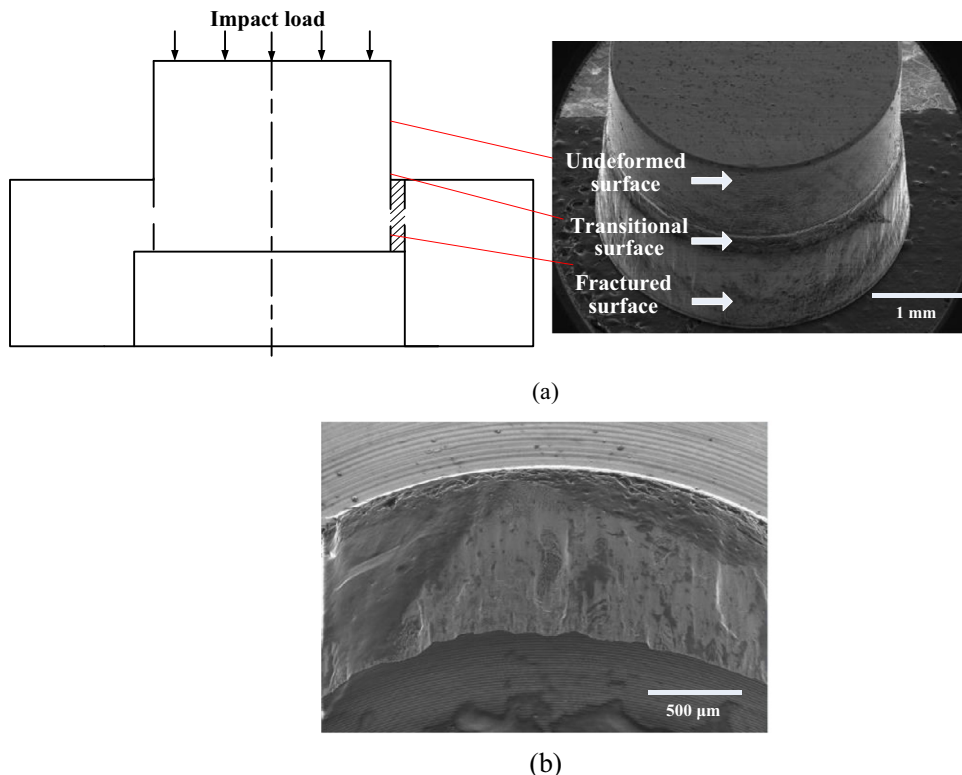


Fig. 9. SEM photographs of the hat-shaped specimen after the SHPB shear test: (a) cylinder part and (b) inner surface of the annulus part.

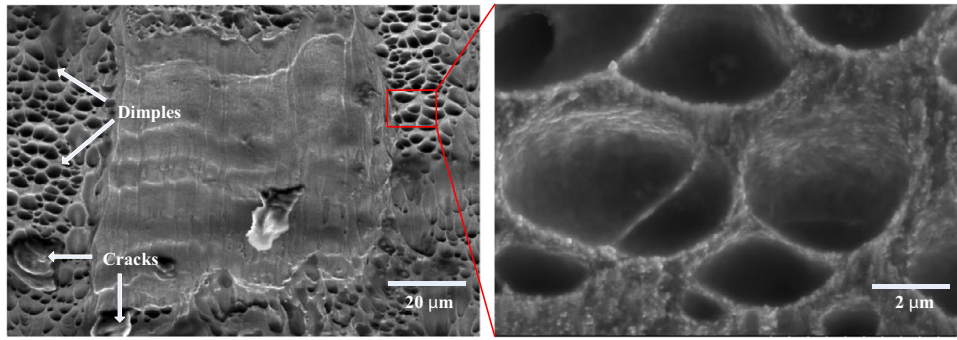


Fig. 10. Micromorphology of the fractured surface after SHPB shear test.

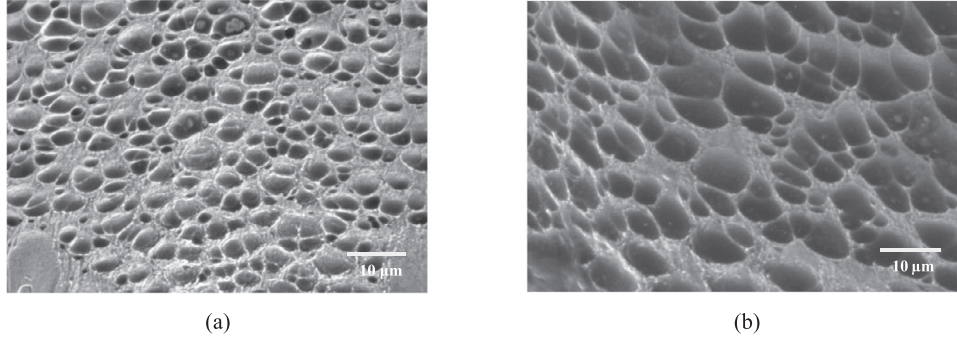


Fig. 11. Dimension of dimples with different shear band widths: (a) 400 μm and (b) 50 μm.

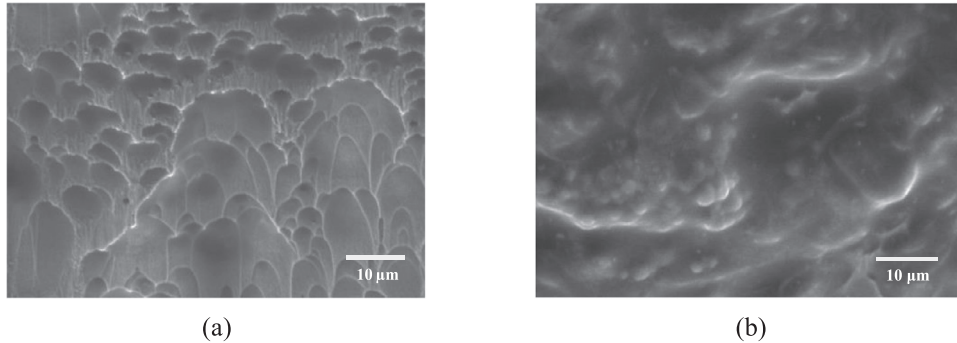


Fig. 12. SEM photographs of melted microdamage: (a) cylinder part and (b) inner surface of the annulus part.

coefficient of the material. Lee and Lin investigated the high temperature deformation behaviour of Ti-6Al-4V alloy by using the split Hopkinson bar test [25]. The specimens were deformed under a constant strain rate of 2000 s^{-1} varying in temperature from 700–1100 °C in intervals of 100 °C [19]. Lee and Lin's J–C constitutive model is shown in Eq. (9).

$$\sigma = [782.7 + 498.4\epsilon^{0.28}] \left[1 + 0.028 \ln\left(\frac{\dot{\epsilon}}{\dot{\epsilon}_0}\right) \right] \left[1 - \left(\frac{T - T_r}{T_m - T_r} \right)^{0.73} \right] \quad (9)$$

Here, parameter C is the strain rate hardening coefficient, which is modified at the ultrahigh strain rate based on the SHPB shear test. The form of Eq. (8) can be changed into the form of the following equation:

$$\frac{\sigma}{A + B\epsilon^n} = \left[1 + C \ln\left(\frac{\dot{\epsilon}}{\dot{\epsilon}_0}\right) \right] \left[1 - \left(\frac{T - T_r}{T_m - T_r} \right)^m \right] \quad (10)$$

Parameter C in Eq. (10) is regarded as the slope of a straight line according to the experimental results at different strain rates.

The value of C is calculated using the least squares method within the 95% confidence range, which results in $C = 0.012$. Then, the J–C constitutive model of titanium alloy Ti-6Al-4V under the ultrahigh strain rate is determined:

$$\sigma = [782.7 + 498.4\epsilon^{0.28}] \left[1 + 0.012 \ln\left(\frac{\dot{\epsilon}}{\dot{\epsilon}_0}\right) \right] \left[1 - \left(\frac{T - T_r}{T_m - T_r} \right)^{0.73} \right] \quad (11)$$

4. Analysis and discussion by FEM simulation

4.1. Analysis of pulse signals in the SHPB shear test

The accuracy of the modified J–C constitutive model is determined, and the validity of the experimental technique is then verified through a finite element method (FEM) simulation. An FEM simulation is performed for all SHPB shear tests using the ABAQUS/Explicit software. The FEM model comprises the striker bar, incident bar, hat-shaped specimen and transmission bar. To reduce

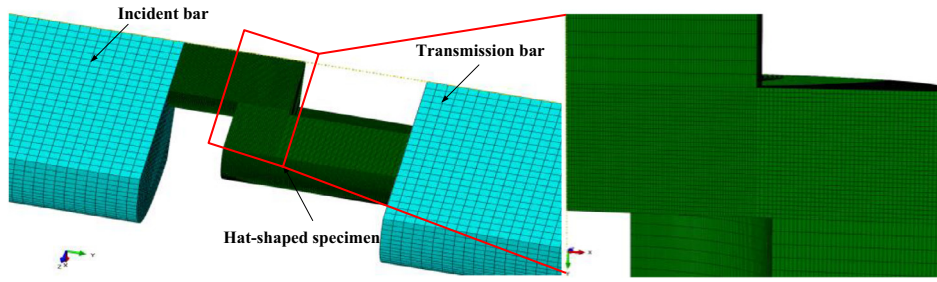


Fig. 13. FEM meshes in the SHPB shear model ($d = 400 \mu\text{m}$).

Table 6

Parameters used in the Johnson–Cook damage model.

d_1	d_2	d_3	d_4	d_5	Melting temperature ($^{\circ}\text{C}$)
−0.090	0.270	−0.480	0.014	3.870	1668

calculation time, the model is simplified by representing only a quarter of specimen. The FEM meshes in the SHPB shear model are shown in Fig. 13. To reduce computation cost, a larger element is used for several parts of the FEM model. An 8-node linear brick, reduced integration, coupled displacement-temperature element (C3D8RT) is selected for the bars, while the completed integration element (C3D8T) is selected for the specimen. The incident bar is partitioned, and the area close to the specimen has a finer mesh density. The specimen consists of 535,613 elements, and the densest mesh is in the shear band (Fig. 13). The dimension of the smallest element in the shear band is 0.025 mm . The striker bar is set as a rigid body, and the others parts are defined as elastic bodies. The material of the incident bar is 18Ni, and the transmission bar is an Al alloy. To consider a thermal softening effect, the step is set to dynamic, temperature-displacement, and explicit. Different thermal values were selected based on the temperatures in the constitutive model (conductivity, inelastic heat fraction and specific heat). The initial field temperature of the bars and specimens are all set to 0°C . The parameters of the J–C constitutive model shown in Eq. (11) are defined in the material plasticity option, which are calculated based on the SHPB shear test. The striker bar, incident bar, specimen and transmission bar are assembled successively, and the energy absorber is simplified into a fixed constraint at the end of the transmission bar.

Several specimens fracture during the SHPB shear test; therefore, Johnson–Cook damage is used in the material (Eq. (12)) (Table 6). Regarding damage evolution, the damage energy output is selected

to determine whether a material fractured. The equation for damage energy in ABAQUS is shown in Eq. (13). The softening type of damage evolution is exponential, and the energy is therefore calculated based on the experimental data.

$$\varepsilon_f^{pl} = \left[d_1 + d_2 \exp\left(d_3 \frac{p}{q}\right) \right] \times \left[1 + d_4 \ln\left(\frac{\dot{\varepsilon}^{pl}}{\dot{\varepsilon}_0}\right) \right] \times \left[1 + d_5 \left(\frac{T - T_r}{T_m - T_r}\right) \right] \quad (12)$$

$$G_f \int_{\bar{\varepsilon}_0^{pl}}^{\bar{\varepsilon}_f^{pl}} L \sigma_y d\bar{\varepsilon}^{pl} \int_0^{\bar{u}_f^{pl}} \sigma_y d\bar{u}^{pl} \quad (13)$$

In Eq. (13), G_f represents the damage energy, L represents the characteristic length, $\bar{\varepsilon}_f^{pl}$ represents the equivalent plastic fractured strain, and \bar{u}_f^{pl} represents the displacement of fracture.

Fig. 14 shows the fracture process of the shear band ($b = 400 \mu\text{m}$, $\dot{\varepsilon}_s = 5.0 \times 10^4 \text{ s}^{-1}$) in the simulation. Once the overall strain energy of an element exceeds the damage energy, that element will be disregarded in the following iteration of the computation as shown in Fig. 14(b). Therefore, this element will be invisible in the deformed specimen. Finally, the specimen with a $400 \mu\text{m}$ shear band width fractured at the $5.0 \times 10^4 \text{ s}^{-1}$ shear strain rate.

To verify the reliability of the numerical simulation, the measured strain pulses shown in Fig. 4(a) are compared with the simulation results ($b = 400 \mu\text{m}$, $\dot{\varepsilon}_s = 5.0 \times 10^4 \text{ s}^{-1}$); the strain pulse results in the FEM model are at the same positions as the strain gauges on the bars. The positions are 55 mm away from the contact surface of specimen and bars. To present a more intuitive comparison between the experiment and simulation results, all values are made positive. Based on Eq. (7), as the incident wave is transferred to the specimen, only the reflected strain and transmission strain need to be verified. Because the fracture process is accounted for, there is good agreement between the duration of the transmission strain signal measured experimentally and in the simulation, as shown in Fig. 15. In addition, before the specimen fractured, the experimental and simulation reflected strain signal had the same tendency, which implies

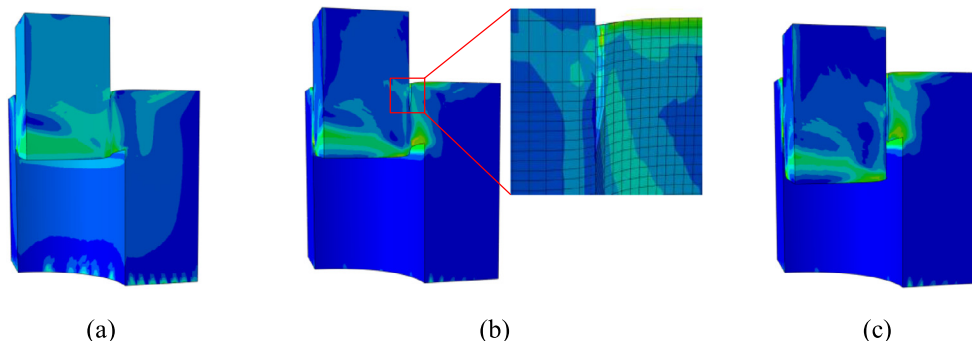


Fig. 14. Fracture process of hat-shaped specimen ($b = 400 \mu\text{m}$, $\dot{\varepsilon}_s = 5.0 \times 10^4 \text{ s}^{-1}$) in the simulation: (a) $286 \mu\text{s}$, (b) $291 \mu\text{s}$, and (c) $318 \mu\text{s}$.

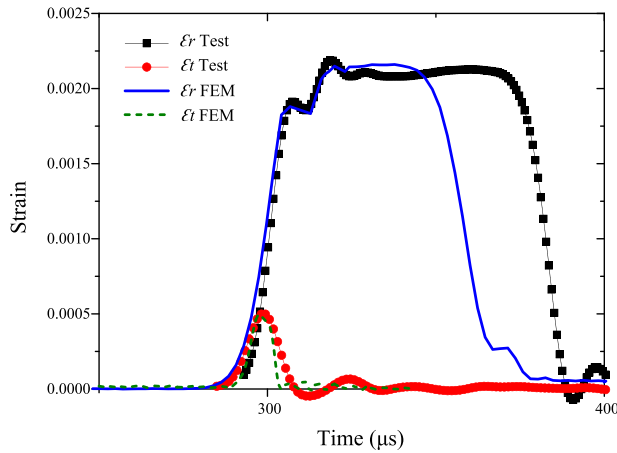


Fig. 15. Comparison of reflected strain and transmission strain between testing and simulation results ($b=400\ \mu\text{m}$, $\dot{\epsilon}_s=5.0 \times 10^4\ \text{s}^{-1}$).

that the overall incident strain signal error in the simulation is very small. The simulation terminates once the incident bar contacts the upper surface of the annulus part of the specimen; therefore, the reflected strain signal in the simulation decreases at approximately $342\ \mu\text{s}$, which is earlier than the experimental result. The comparison of the experimental and simulation reflected strain and transmission strain show that the numerical simulation is in good agreement with the actual SHPB shear test.

4.2. Analysis of stress–strain relationship

Before processing the stress–strain curves, the deformation mode of the SHPB shear test is analysed. The principal major and minor strain in the simulation is shown in Fig. 16. The ratio of the principal major and minor strains is -1 , which implies that the test is a process of pure shear. It is proved that the SHPB shear test can be used to test the dynamic shear behaviour of titanium Alloy Ti-6Al-4V at high strain rates. Moreover, the shear strain in the SHPB shear test ($b=400\ \mu\text{m}$, $\dot{\epsilon}_s=5.0 \times 10^4\ \text{s}^{-1}$) is compared with the simulation average data of shear band in Fig. 17. After linear fitting, the slope of the straight line represents the shear strain rate. The error between nominal shear strain rate and assumption values before tests is little. Moreover, the slope of simulation is greater than that of the test owing to the existence of energy loss in real tests.

The temperature nephogram of the simulation ($b=400\ \mu\text{m}$, $\dot{\epsilon}_s=5.0 \times 10^4\ \text{s}^{-1}$) is obtained to study the temperature distribution in the SHPB shear test (Fig. 18). When the shear zone is about to break completely, the temperature reaches a maximum of $1705\ ^\circ\text{C}$; the maximum plastic deformation work is achieved in the shear band, and the temperature reaches a maximum value as the heat cannot be diffused inside the shear zone. Moreover, $1705\ ^\circ\text{C}$ exceeds

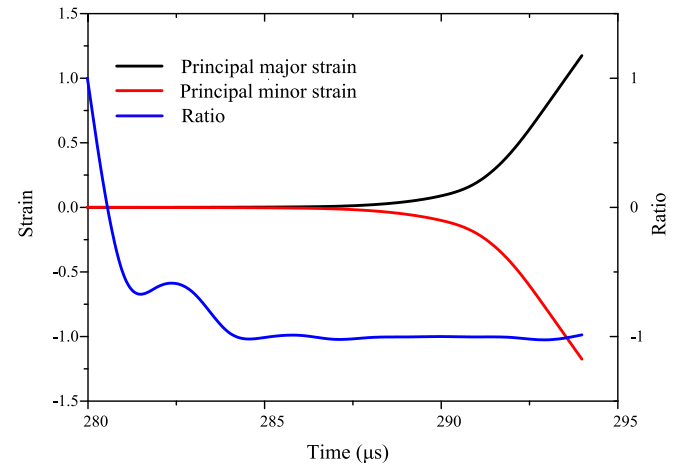


Fig. 16. Principal major and minor strain of shear band in the simulation ($b=400\ \mu\text{m}$, $\dot{\epsilon}_s=5.0 \times 10^4\ \text{s}^{-1}$).

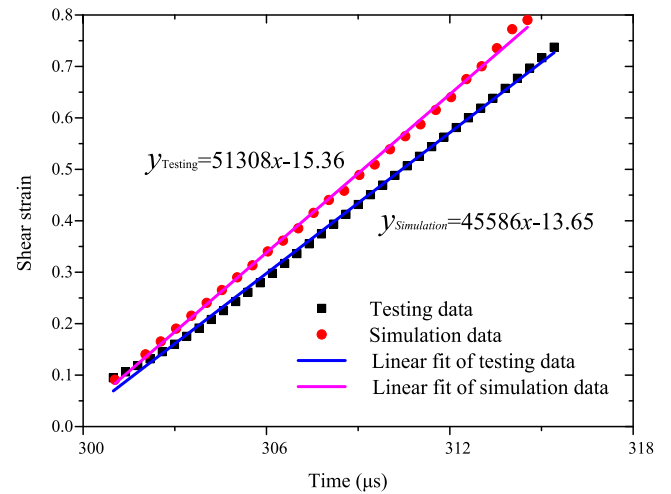


Fig. 17. Comparison of linear fits of strain-time curves from the test and simulation ($b=400\ \mu\text{m}$, $\dot{\epsilon}_s=5.0 \times 10^4\ \text{s}^{-1}$).

the melting point of titanium Alloy Ti-6Al-4V ($1668\ ^\circ\text{C}$), which implies that the local shear band is likely melted. This conclusion proves the existence of the thermal softening effect mentioned above. The SEM photograph of the melted micro-damage is also in agreement with this conclusion.

A comparison of the experimental results and the simulation results based on Lee and Lin's J–C constitutive model (Eq. (9)) and the modified model (Eq. (11)) with different shear band widths and shear strain rates are shown in Fig. 19; it is evident that the parameters in the J–C constitutive model need to be changed. A small stress

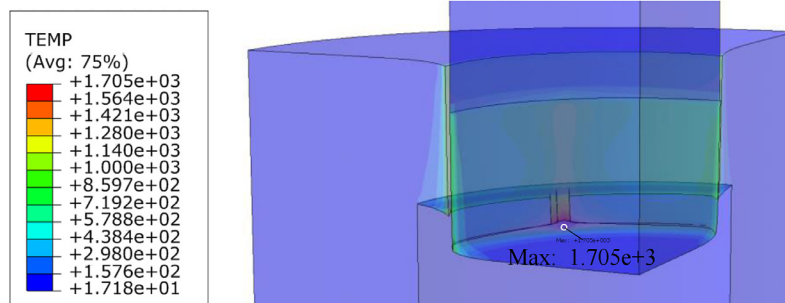


Fig. 18. Temperature nephogram of simulation ($b=400\ \mu\text{m}$, $\dot{\epsilon}_s=5.0 \times 10^4\ \text{s}^{-1}$).

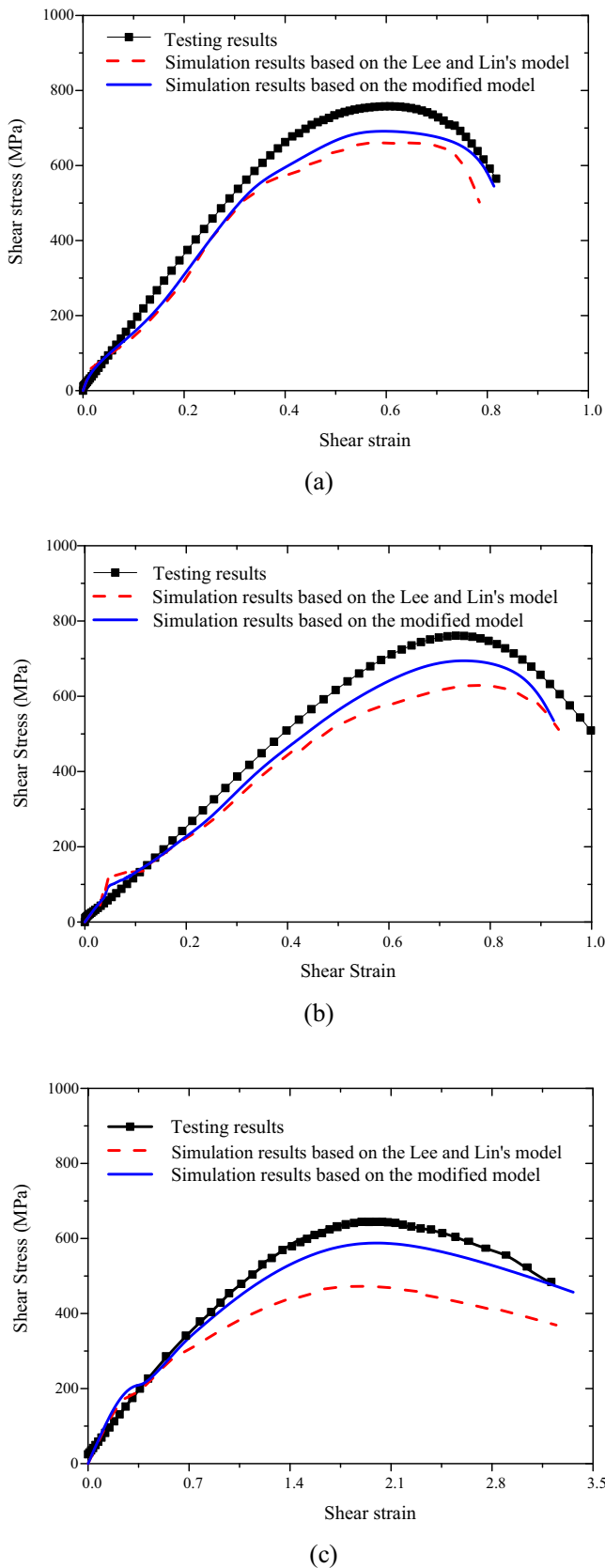


Fig. 19. Comparison between experimental and simulation results under different conditions: (a) T3 ($b = 400 \mu\text{m}$, $\dot{\gamma}_s = 5.0 \times 10^4 \text{ s}^{-1}$), (b) T6 ($b = 200 \mu\text{m}$, $\dot{\gamma}_s = 5.0 \times 10^4 \text{ s}^{-1}$), and (c) T11 ($b = 50 \mu\text{m}$, $\dot{\gamma}_s = 3.0 \times 10^5 \text{ s}^{-1}$).

fluctuation is observed in the simulation results with a small strain, owing to the initial unstable pulse signals. Under the ultrahigh strain rate, the results show that the simulation of Lee and Lin's constitutive model does not agree with the experimental results, which proves that Lee and Lin's J–C constitutive model has limitations, especially when the shear band width is very small ($50 \mu\text{m}$). In addition, there is more variation in the simulation results based on Lee and Lin's J–C constitutive model with an increasing shear strain rate. Conversely, the simulation results of the modified constitutive model agree with the experimental results, and the accuracy is higher with the increasing shear strain rate. The modified J–C constitutive model applies to dynamic shear testing at the ultrahigh strain rate.

5. Conclusion

In this study, the SHPB technology is implemented to characterize the dynamic properties of titanium alloy Ti-6Al-4V at high and ultrahigh strain rates. The size effects were studied by improving the specimen structure for the SHPB shear test to obtain different shear band widths. Based on the shear testing results, the J–C constitutive model of titanium alloy Ti-6Al-4V at an ultrahigh strain rate is modified.

- (1) In the SHPB compression and shear tests, titanium alloy Ti-6Al-4V exhibit an obvious strain rate hardening effect. The adiabatic shear band is formed with the presence of a high inner temperature due to the large plastic deformation in a short period. As the strain rate increases, thermal softening became the dominant effect among the competing mechanisms.
- (2) A size effect of the shear band width is found in the shear test. The shear strain corresponding to the ultimate shear stress with a shear band width of $50 \mu\text{m}$ is much larger than those of $400 \mu\text{m}$ and $200 \mu\text{m}$.
- (3) The J–C constitutive model of titanium alloy Ti-6Al-4V at an ultrahigh strain rate is modified. A numerical simulation of the SHPB shear test is conducted using ABAQUS; the simulation results for the pulse signals, shear strain rate and shear stress-strain curves agree with the experimental SHPB shear test. Based on the simulation results, the modified J–C constitutive model is more accurate than Lee and Lin's model.

Acknowledgements

This work has been financed by National Natural Science Foundation of China (no. 51375050) and Fok Ying-Tong Education Foundation for Young Teachers in the Higher Education Institutions of China (no. 151052).

References

- [1] Brousseau EB, Dimov SS, Pham DT. Some recent advances in multi-material micro- and nano-manufacturing. *Int J Adv Manuf Tech* 2010;47(1–4):161–80.
- [2] Bruschi S, Poggio S, Quadrini F, Tata ME. Workability of Ti-6Al-4V alloy at high temperatures and strain rates. *Mater Lett* 2004;58(27–28):3622–9.
- [3] Xue Q, Gray GT. Development of adiabatic shear bands in annealed 316 L stainless steel: part I. Correlation between evolving microstructure and mechanical behavior. *Metall Mater Trans A* 2005;36(6):1471–86.
- [4] Anand L. Moderate deformations in extension-torsion of incompressible isotropic elastic materials. *J Mech Phys Solids* 1986;28(2):293–304.
- [5] Pei CH, Li ZX, Fan QB, Huang X. Quasi-static tensile mechanical property of TC6 titanium alloy under low direct current Material. *Mater Res Innov* 2014;8 (S4): S4-198-S4-201.
- [6] Mohammadhosseini A, Masood SH, Fraser D, Jahedi M. Dynamic compressive behaviour of Ti-6Al-4V alloy processed by electron beam melting under high strain rate loading. *Adv Manuf* 2015;3(3):232–43.
- [7] Wang BL, Ai X, Liu ZQ, Liu JG. Plastic flow modeling of Ti-5Al-2Sn-2Zr-4Mo-4Cr alloy at elevated temperatures and high strain rates. *J Wuhan Univ Technol* 2015;30(3):611–6.

- [8] Daryadel SS, Mantena PR, Kim K, Stoddard D, Rajendran AM. Dynamic response of glass under low-velocity impact and high strain-rate SHPB compression loading. *J Non Cryst Solids* 2015.
- [9] Peirs J, Verleysen P, Paepegem WV, Degrieck. Determining the stress–strain behaviour at large strains from high strain rate tensile and shear experiments. *Int J Impact Eng* 2011;38(5):406–15.
- [10] Zhang CQ, Xie LS, Chen MH, Shang QG. Dynamic mechanical property and plastic constitutive relation of tc4-dt Ti alloy under high strain rate. *Chin J Nonferr Metal* 2015;25(2):323–9.
- [11] Mines RAW. A one-dimensional stress wave analysis of a lightweight composite armour. *Compos Struct* 2004;64(1):55–62.
- [12] Mohr D, Gary G, Lundberg B. Evaluation of stress–strain curve estimates in dynamic experiments. *Int J Impact Eng* 2010;37(2):161–9.
- [13] Wu QS. Effect of temperature and strain rate on mechanical behaviors of low alloy steel. *J Mater Sci Mater El* 2015;3(3):232–43.
- [14] Yang LM, Shim VPW. An analysis of stress uniformity in split Hopkinson bar test specimens. *Int J Impact Eng* 2005;31(2):129–50.
- [15] Verleysen P, Degrieck J. Experimental investigation of the deformation of Hopkinson bar specimens. *Int J Impact Eng* 2014;86(3):239–53.
- [16] Becze CE. A thermo-mechanical force model for machining hardened steel. Canada: McMaster University (Canada); 2003.
- [17] Meyer LW, Manwaring S. Metallurgical applications of shock-wave and high-strain rate phenomena. In: Murr LE, editor. NY: Marcel Dekker Inc; 1986.
- [18] Nie ZG, Wang G, Yu JC, Liu DH, Rong YM. Phase-based constitutive modeling and experimental study for dynamic mechanical behavior of martensitic stainless steel under high strain rate in a thermal cycle. *Mech Mater* 2016;101:160–9.
- [19] Xu ZJ, Ding XY, Zhang WQ, Huang FL. A novel method in dynamic shear testing of bulk materials using the traditional SHPB technique. *Int J Impact Eng* 2017;101:90–104.
- [20] Zhao JW, Ding H, Hou HL, Li ZQ. Influence of hydrogen content on hot deformation behavior and microstructural evolution of Ti600 alloy. *J Alloy Compd* 2010;491(1–2):673–8.
- [21] Rastegari HA, Asgari S, Abbasi SM. Producing Ti–6Al–4V/TiC composite with good ductility by vacuum induction melting furnace and hot rolling process. *Mater Des* 2011;32(10):5010–4.
- [22] Rizal S, Homma H. Dimple fracture under short pulse loading. *Int J Impact Eng* 2000;24(1):69–83.
- [23] Glezer AM. On the nature of ultrahigh plastic (megaplastic) strain. *Bull Russ Acad Sci Phys* 2007;71(12):1722–30.
- [24] Johnson GR, Cook WH. A constitutive model and data for metals subjected to large strains, high strain rates and high temperatures. In: Processing of the seventh international symposium on ballistics; 1983. p. 541–7.
- [25] Lee WS, Lin CF. High-temperature deformation behaviour of Ti-6Al-4V alloy evaluated by high strain-rate compression tests. *J. Mater. Process. Tech* 1998;75(1–3):127–36.